Radio Science, Volume 28, Number 6, Pages 1111–1130, November–December 1993

Polarimetric remote sensing of geophysical medium structures

S. V. Nghiem, S. H. Yueh, R. Kwok, and D. T. Nguyen

Jet Propulsion Laboratory, California Institute of Technology, Pasadena, California

(Received July 23, 1992; revised December 29, 1992; accepted May 17, 1993.)

Polarimetric remote sensing of structures in geophysical media is studied in this paper based on their symmetry properties. Orientations of spheroidal scatterers described by spherical, uniform, planophile, plagiothile, erectophile, and extremophile distributions are considered to derive their polarimetric backscattering characteristics. These distributions can be identified from the observed scattering coefficients by comparison with theoretical symmetry calculations. A new parameter is defined to study scattering structures in geophysical media. Experimental observations from polarimetric data acquired by the Jet Propulsion Laboratory airborne synthetic aperture radar over forests, sea ice, and sea surface are presented to illustrate the use of symmetry properties. For forests, the coniferous forest in Mount Shasta area and mixed forests near Presque Isle show evidence of the centrical symmetry at C band. In sea ice from the Beaufort Sea, multiyear sea ice has a cross-polarized ratio e close to e_0, calculated from symmetry, due to the randomness in the scattering structure. For first-year sea ice, e is much smaller than e_0 as a result of preferential alignment of the columnar structure of the ice. From polarimetric data of a sea surface in the Bering sea, it is observed that e and e_0 are increasing with incident angle and e is greater than e_0 at L band because of the directional feature of sea surface waves. Use of symmetry properties of geophysical media for polarimetric radar calibration is also suggested.

1. INTRODUCTION

Symmetry properties of geophysical media have been utilized to study the characteristics of the corresponding covariance matrices [*Nghiem et al.*, 1992]. Relationships among polarimetric backscattering coefficients in the covariance matrices have been derived from reflection, rotation, azimuthal, and centrical symmetry groups. Theoretical models for volume and surface scatterings have been shown to be consistent with these relationships. Calculations from the symmetry properties can be used as a reference to investigate scattering structures in geophysical media. Directional surface features can be detected based on the deviation of the scattering coefficients from the symmetry behavior. Orientation distributions of nonspherical scatterers can be identified and classified by comparing the polarimetric scattering coefficients with the symmetry response.

Geophysical media have certain symmetry properties which manifest themselves statistically in polarimetric scattering coefficients. For example, wind-generated waves on ocean surfaces have reflection symmetry with respect to the vertical plane parallel to the wind direction [*Stewart*, 1985]. This reflection symmetry decorrelates the copolarized and the cross-polarized elements in the backscattering matrix of the ocean surface and thereby forces the values of the corresponding scattering coefficients to vanish [*Nghiem et al.*, 1992]. These scattering coefficients become nonzero and vary periodically with azimuthal angle and return to the zero value again when the azimuthal direction coincides with the wind direction. First-year sea ice has brine inclusions preferentially aligned in the vertical direction [*Weeks and Ackley*, 1982], while scatterers in multiyear ice are more randomly distributed. The symmetry calculations provide references for comparing polarimetric returns from sea ice to unveil the structural information which can help identify ice types. In agricultural fields, plants are usually grown in a row structure which has reflection symmetry about a vertical plane perpendicular or parallel to the row direction from which the expected scattering coefficients σ_{hhhv} and σ_{hvvv} are zero. Azimuthal symmetry with vertical axis of symmetry is often observed in forests [*Le Toan et al.*, 1990], whose scattering coefficients are restricted by the relationships imposed by this symmetry. Inclination angles of vegetation elements have been formulated with probability density functions to describe the

Paper number 93RS01376.
0048-6604/93/93RS-01376$08.00

scatterer orientations including spherical, uniform, planophile, plagiothile, erectophile, and extremophile distributions [*Goel and Strebel*, 1984], which are dependent on environmental factors such as wind, rain, or plant stress.

To obtain structural information from polarimetric remote sensing data, an investigation of the covariance matrices for various distributions is necessary. Polarimetric data collected from experimental campaigns with the Jet Propulsion Laboratory (JPL) synthetic aperture radar (SAR) over forests, sea ice, sea surfaces, and other geophysical media are used to illustrate the behaviors of different structures. In this paper, we will consider coniferous forest in Mount Shasta area and mixed forest near Presque Isle, first-year and multiyear sea ice in the Beaufort sea, and a sea surface which was imaged during a flight over the Bering Sea. Retrieval of structural information in polarimetric data is illustrated by comparing experimental data with symmetry behavior of the scattering coefficients. Evidence of symmetry properties in natural targets can also be used to select distributed targets for polarimetric radar calibration.

This paper is organized into five sections. Section 2 reviews the symmetry properties of polarimetric backscattering coefficients for media with reflection, rotation, azimuthal, and centrical symmetries. Section 3 presents various orientation distributions of scatterers for which the scattering coefficients are calculated and then compared with the symmetry behaviors. Section 4 presents experimental observations from the polarimetric data at P, L, and C band frequencies obtained with the airborne JPL SAR over forests, sea ice, and sea surface. From this analysis, geophysical media with centrical symmetry are identified as possible targets for use in calibration of remote sensing polarimetric radars. Section 5 concludes the paper.

2. SYMMETRY PROPERTIES

Interrelations among polarimetric backscattering coefficients have been derived [*Nghiem et al.*, 1992] for both reciprocal and nonreciprocal geophysical media with reflection, rotation, azimuthal, and centrical symmetry properties. The symmetry groups can be constructed from three fundamental operations: mirror reflection, axial rotation, and linear translation. The derivations are based on the invariance under symmetry transformations in the linear polarization basis. The derived results are valid for volume scattering, surface scattering, or volume-surface interactions to all scattering orders or to the total scattering effects no matter how dense the medium or how rough the surface is, as long as the scattering configuration has the corresponding symmetry. These symmetries impose restrictions among polarimetric scattering coefficients and thus reduce the number of independent parameters in the covariance matrix and also the Mueller matrix as summarized in Table 1. The results derived from the symmetry considerations are briefly reviewed in the following paragraphs for convenience and clarity of subsequent discussions.

TABLE 1. Number of Independent Parameters in Covariance or Mueller Matrix

	Nonreciprocal	Reciprocal
No symmetry	16	9
Reflection	8	5
Rotation	6	3
Azimuthal (normal)	3	2
Centrical (oblique)	3	2

Reflection symmetry group with respect to a vertical plane contains the mirror reflection transformation denoted by σ_v, where the subscript v stands for vertical, in the notation of Group theory [*Hamermesh*, 1972]. Such symmetry is observed on wind-generated water waves, where vertical plane of the symmetry is parallel to the downwind or upwind direction. The reflection symmetry imposes the complete decorrelation between copolarized and cross-polarized elements in the scattering matrix leading to the following results:

$$\sigma_{hhhv} = \sigma_{hvhh} = \sigma_{vvvh} = \sigma_{vhvv} = 0 \qquad (1a)$$

$$\sigma_{hhvh} = \sigma_{vhhh} = \sigma_{vvhv} = \sigma_{hvvv} = 0 \qquad (1b)$$

Pure rotation symmetry in the two-dimensional linear polarization basis has an axis of symmetry as seen by, for instance, field-aligned wave propagation in the Earth ionosphere, which is a plasma magnetized by the geometric field. Transformations in rotation symmetry group are labeled by the continuous rotation angle α and denoted by C_∞, according to Group theory notation [*Hamermesh*, 1972]. This symmetry requires the scattering coefficients to satisfy a number of relationships as expressed explicitly in equations (34)–(38) of the paper by *Nghiem et al.* [1992].

Azimuthal symmetry has an axis of symmetry as in the case of a normal incident wave on a random rough surface or a layer of randomly oriented scatterers. The azimuthal symmetry group, denoted by $C_{\infty v}$, can be obtained from the rotation group C_∞ by adjoining the reflection σ_v in any vertical plane passing through the rotational axis of symmetry. Thus azimuthal symmetry inherits the characteristics from both the reflection and the rotation symmetries. The combination of the results from the two symmetries provides the interrelationships among the scattering coefficients of a medium with azimuthal symmetry. Furthermore, when a medium with the azimuthal symmetry is also reciprocal, the nonzero scattering coefficients are constrained by the following interrelations:

$$\sigma_{hhhh} = \sigma_{vvvv}, \qquad \text{Im } \sigma_{hhvv} = 0,$$
$$\sigma_{hvhv} = (\sigma_{hhhh} + \sigma_{vvvv} - 2\text{Re } \sigma_{hhvv})/4 \tag{2a}$$

or

$$\gamma = 1, \qquad \text{Im } \rho = 0, \qquad e = (1 + \gamma - 2\text{Re } \rho)/4 \tag{2b}$$

where (2*b*) is the normalized form of (2*a*) with $\sigma = \sigma_{hhhh}$, $\gamma = \sigma_{vvvv}/\sigma$, $e = \sigma_{hvhv}/\sigma$, and $\rho = \sigma_{hhvv}/(\sigma\sqrt{\gamma})$. The relationships in (2) hold for all scattering mechanisms when the wave is at normal incidence to layer random media without directional features in azimuth. For oblique incidence the azimuthal symmetry degenerates to the reflection symmetry, since the observation direction is not parallel to the azimuthal symmetry axis.

Centrical symmetry has a point of symmetry as visualized by randomly oriented scatterers like leaves, for example, with spherical orientation distribution in a vegetation canopy. Centrical symmetry also has reflection symmetry about any plane containing the point of symmetry and azimuthal symmetry about any axis passing through the symmetry point. All symmetry relationships among the polarimetric backscattering coefficients presented in the previous paragraphs are therefore valid at all azimuthal and incident angles including oblique cases. The behavior of the centrical symmetry can therefore be used as a reference to study the scatterer structures described by various probability density functions of orientations.

3. ORIENTATION DISTRIBUTIONS

The constraints on the polarimetric backscattering coefficients have been reviewed in the above section for symmetry properties which are often encountered in geophysical media. These symmetries are related to the structural characteristics of the medium under consideration. Scatterers in geophysical media tend to structure themselves in a certain statistical manner. Ocean waves driven by wind are directional and cause the periodicity on radar backscatterers in azimuthal angles [*Stewart*, 1985]. Sea ice grows vertically downward in columnar structure [*Weeks and Ackley*, 1982] under quiescent conditions with *c* axes horizontal and brine inclusions preferentially vertical. Interestingly, it has been observed that scatterers, such as vegetation elements in a canopy, are oriented symmetrically in azimuthal directions [*Le Toan et al.*, 1990] and distributed at inclination angles with several special distributions describing major types of plant canopies [*Goel and Strebel*, 1984].

Nonspherical scatterers can be classified into needlelike shapes, as seen on leaves of many coniferous trees or disklike shapes, as observed in leaves of many deciduous trees. The distribution of scatterer orientations is dependent on the scatterer species, environmental effects, and physiological states. For species with no azimuthal preference, several distributions have been reported including spherical, uniform, planophile, plagiothile, erectophile, or extremophile distributions [*Goel and Strebel*, 1984, and references therein]. Probability density functions of the scatterer orientations are given in terms of inclination angles θ from 0 to 90°. For a needle the inclination angle is between the major axis of the needle and the horizontal plane [*Kimes et al.*, 1979]. For a disk the inclination angle is the zenith angle of the vector normal to the upper surface of the disc [*Goel and Strebel*, 1984] or, equivalently, the angle between the plane of the disk and the horizontal plane. These orientation distributions have certain symmetries which are examined in this section to study their effects on the scattering coefficients for practical applications in polarimetric remote sensing.

The scattering coefficients presented in the following subsections are calculated from the correlations of backscattered field of spheroidal scatterer with a prescribed orientation distribution function. The scattering matrix is obtained by using the

quasi-static approximation for the internal induced current for small ellipsoids [*Tsang et al.*, 1985 section 4.3, chapter 3]. In this case the cross-polarized return is due to the nonspherical shape of the scatterers. For each distribution type the ratio $e = \sigma_{hvhv}/\sigma$ from the model is compared with the quantity

$$e_0 = (1 - |\rho|)/2 \tag{3}$$

defined as suggested by the centrical symmetry, where ρ is also obtained from the model as a function of incident angles. Centrical symmetry can thus be detected for the scatterer orientation, whose polarimetric response is such that $e = e_0$ at arbitrary incident angles. The deviation of e from e_0 therefore indicates how the scatterers are structured as discussed in the following subsections.

3.1. *Spherical Distribution*

Spherical distribution of orientation is used to describe scatterers with completely random orientation. The probability density and distribution functions for this type of structure are

Density

$$p(\theta) = \sin\theta \tag{4a}$$

Distribution

$$P(\theta) = 1 - \cos\theta \tag{4b}$$

respectively. The probability density function for disc orientation is plotted in polar coordinates as a function of inclination angle in Figure 1*a* where the solid dots denote values of the density for inclination angles from 0 to $\pi/2$ (0°, 90°); the open circles are used to complete the plot at other inclination angles for pictorial illustration of the orientation. For needles, cosine function of inclination angle should be used for the probability density function.

Consider a region containing nonspherical scatterers with permittivity $\varepsilon = (30 + i10)\varepsilon_0$ at wave frequency of 5.3 GHz. The scatterers have random orientation as depicted by (4). Polarimetric backscattering coefficients are calculated from the model [*Tsang et al.*, 1985] for prolate spheroidal shapes (needlelike) with semiaxial lengths $a = 0.1$ mm and $b = 2.5$ mm and also for oblate spheroidal shapes (disklike) with $a = 2.5$ mm and $b = 0.1$ mm. To compare with e, e_0 is obtained from (3). The results are shown in Figure 2 for needlelike and Figure 3 for disklike scatterers. In both cases the behavior of the polarimetric parameters are similar and insensitive to incident angles. For the spherical distribution, $\gamma = 1$, $e = e_0$, and ρ is real at all incident angles. Thus needlelike and disklike scatterers with spherical orientation distribution exhibit the behavior of centrical symmetry.

3.2. *Uniform Distribution*

Uniform distribution of orientation characterizes scatterers, whose proportion is the same at all angles. For this type of orientation the probability density and distribution functions are simply

Density

$$p(\theta) = 2/\pi \tag{5a}$$

Distribution

$$P(\theta) = 2\theta/\pi \tag{5b}$$

In Figure 1*b*, the uniform probability density is plotted in polar coordinates as a function of inclination angle. The range from 0 to $\pi/2$ (0°, 90°) is indicated by the solid dots in the plot.

As in the last subsection, scatterers with permittivity $\varepsilon = (30 + i10)\varepsilon_0$ at 5.3 GHz are considered in order to calculate the scattering with the theoretical model. Values of ratio e between cross-polarized return σ_{hvhv} and copolarized return σ_{hhhh} are then obtained and compared with e_0, as computed from the symmetry formula. The results for needlelike scatterers are shown in Figure 4. While γ is insensitive to the incident angle in the case of spherical distribution, the uniform distribution has γ increasing, when the incident angle becomes more oblique, as observed from Figure 4(top). Compared to the symmetry values of e_0, ratio e from the model is the same at normal incidence as a result of the azimuthal symmetry and becomes higher at larger incident angles as seen in Figure 4(bottom). For disklike scatterers, the results in Figure 5(top) indicate that γ decreases as the incident angle increases. As opposed to the case of needles, ratio e

Fig. 1. (Opposite) Probability density functions for scatterer orientations versus inclination angle. (*a*) Spherical probability density, (*b*) uniform probability density, (*c*) planophile probability density, (*d*) plagiothile probability, (*e*) erectophile probability density, and (*f*) extremophile probability density.

(a) Spherical Probability Density

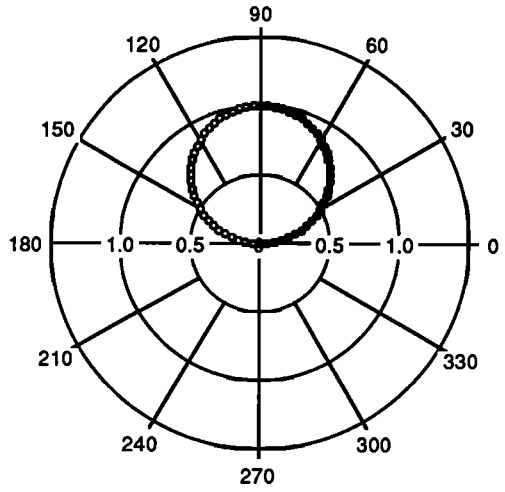

(b) Uniform Probability Density

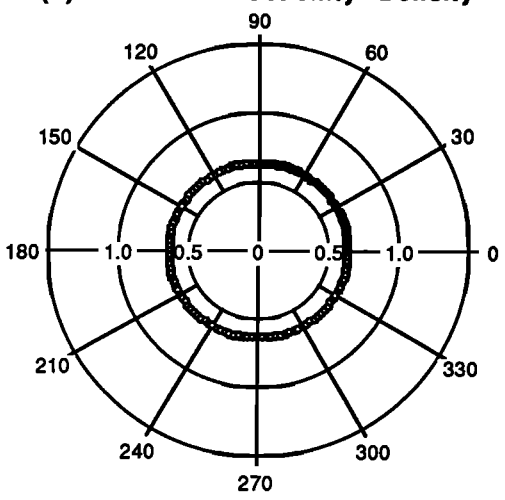

(c) Planophile Probability Density

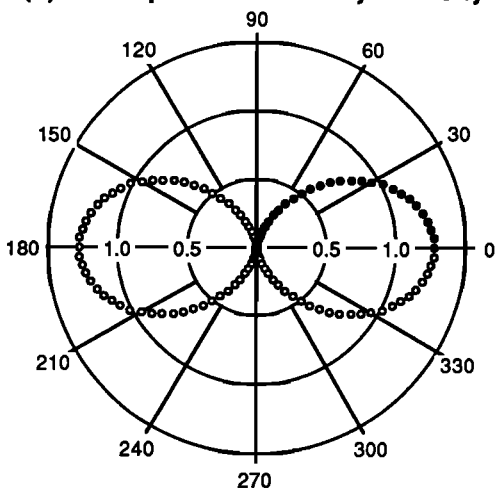

(d) Plagiothile Probability Density

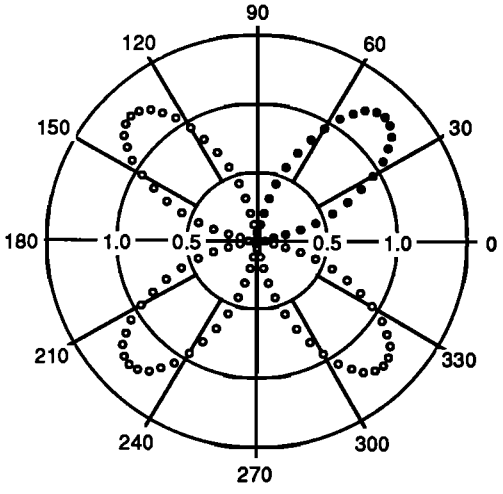

(e) Erectophile Probability Density

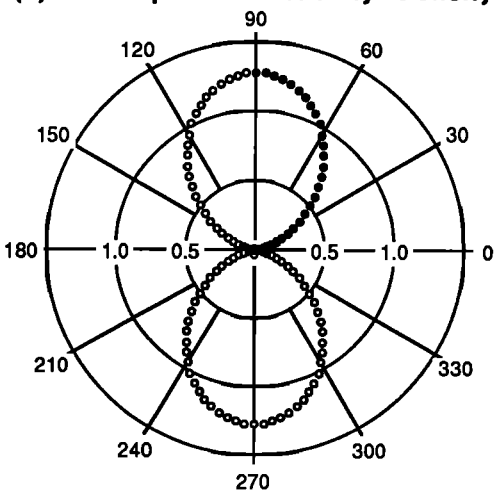

(f) Extremophile Probability Density

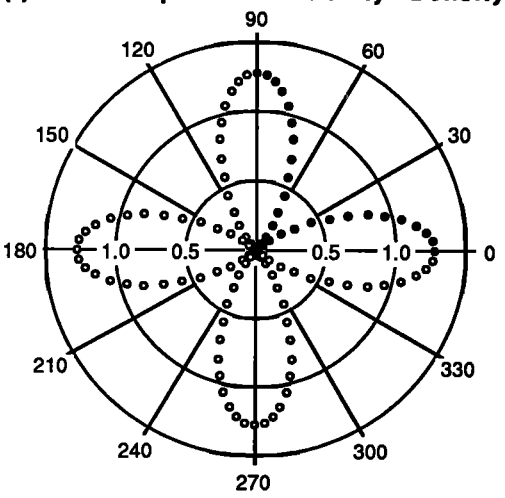

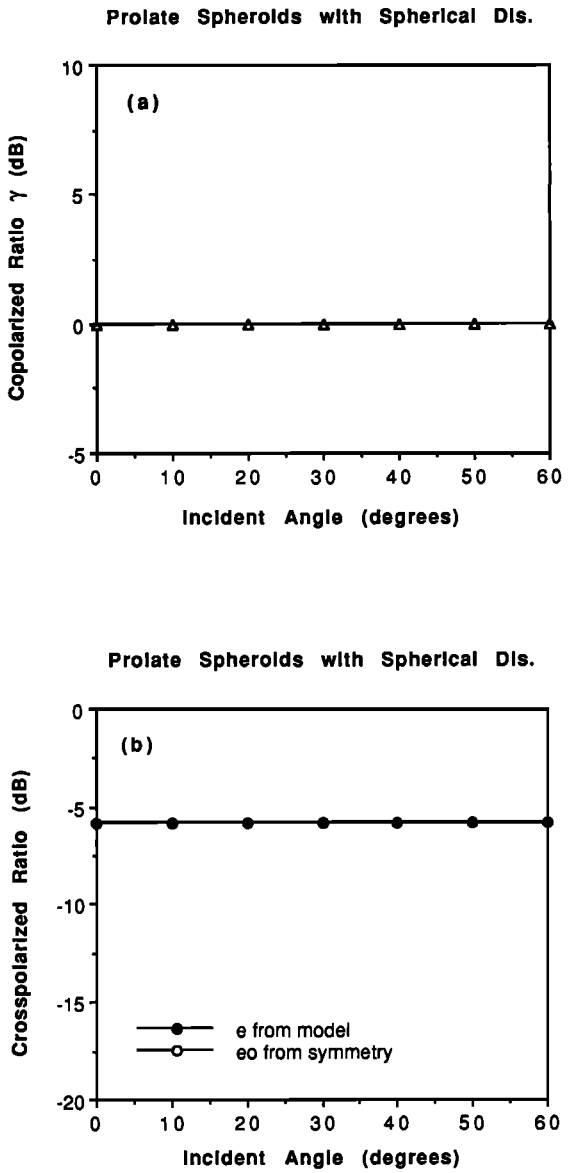

Fig. 2. Polarimetric response of prolate spheroids with spherical distribution of orientation.

for discs is lower than e_0 as observed from Figure 5(bottom).

3.3. *Planophile Distribution*

Planophile distribution of orientation describes scatterers whose horizontal orientation is most frequent. The probability density and distribution functions are expressed in terms of inclination angle as

Density

$$p(\theta) = 2(1 + \cos 2\theta)/\pi \tag{6a}$$

Distribution

$$P(\theta) = (2\theta + \sin 2\theta)/\pi \tag{6b}$$

In polar coordinates the probability density function (6*a*) is plotted as a function of inclination angle in Figure 1*c*, where the solid dots denote values of

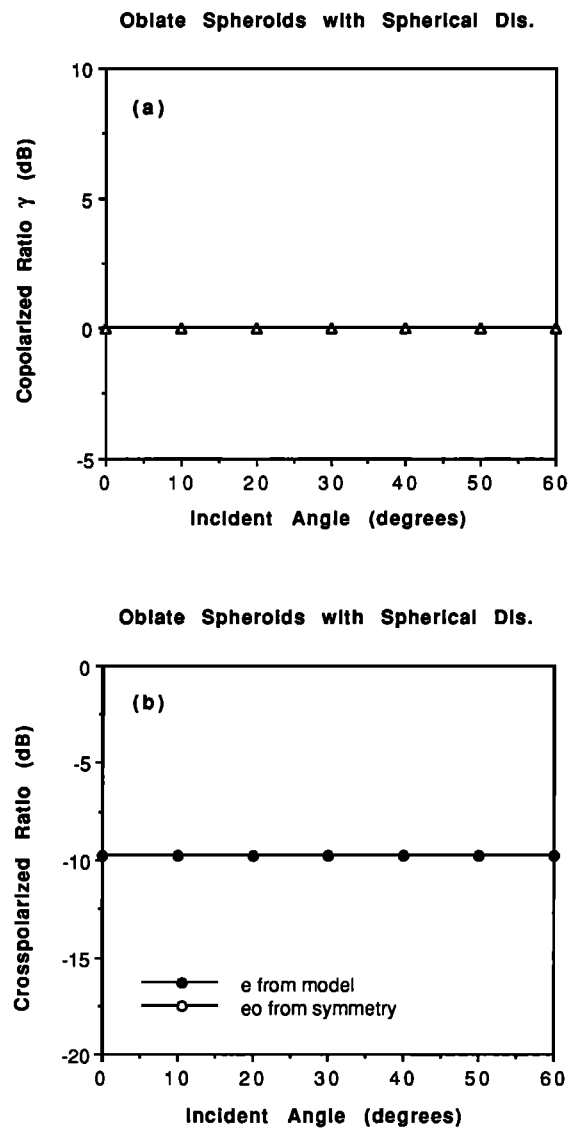

Fig. 3. Polarimetric response of oblate spheroids with spherical distribution of orientation.

the density for inclination angles from 0 to $\pi/2$ (0°, 90°).

Scatterers with permittivity $\varepsilon = (30 + i10)\varepsilon_0$ at 5.3 GHz are considered as in the last subsection to obtain the scattering coefficients from the model, and then e_0 is calculated. The results are presented in Figure 6 for needlelike scatterers and in Figure 7 for disklike scatterers. For both shapes of the scatterers, planophile distribution of orientation renders γ decreased for increased incident angle

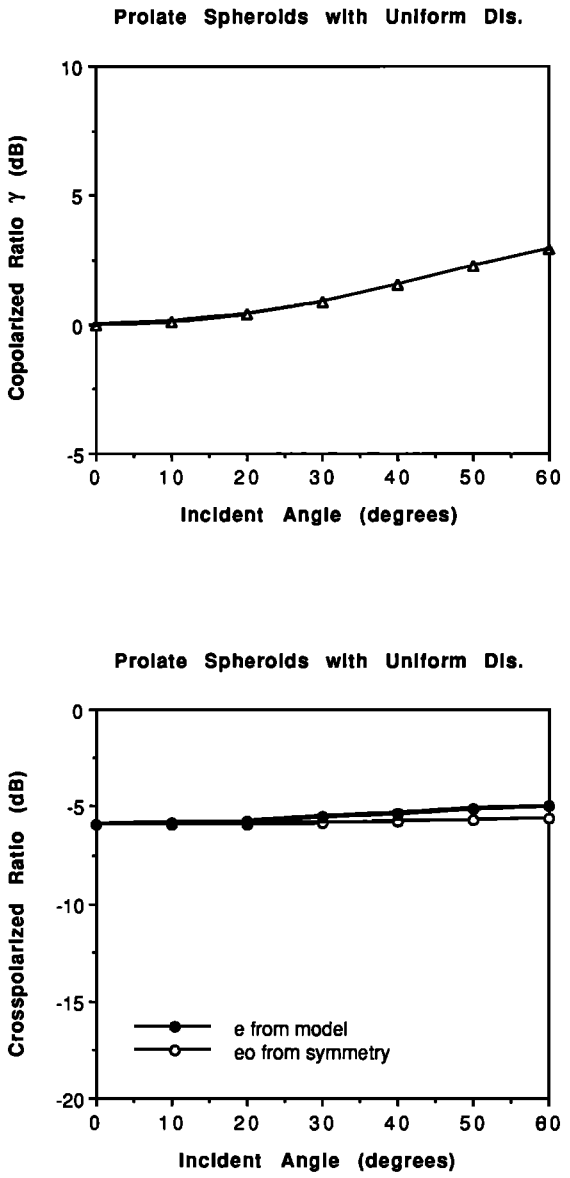

Fig. 4. Polarimetric response of prolate spheroids with uniform distribution of orientation.

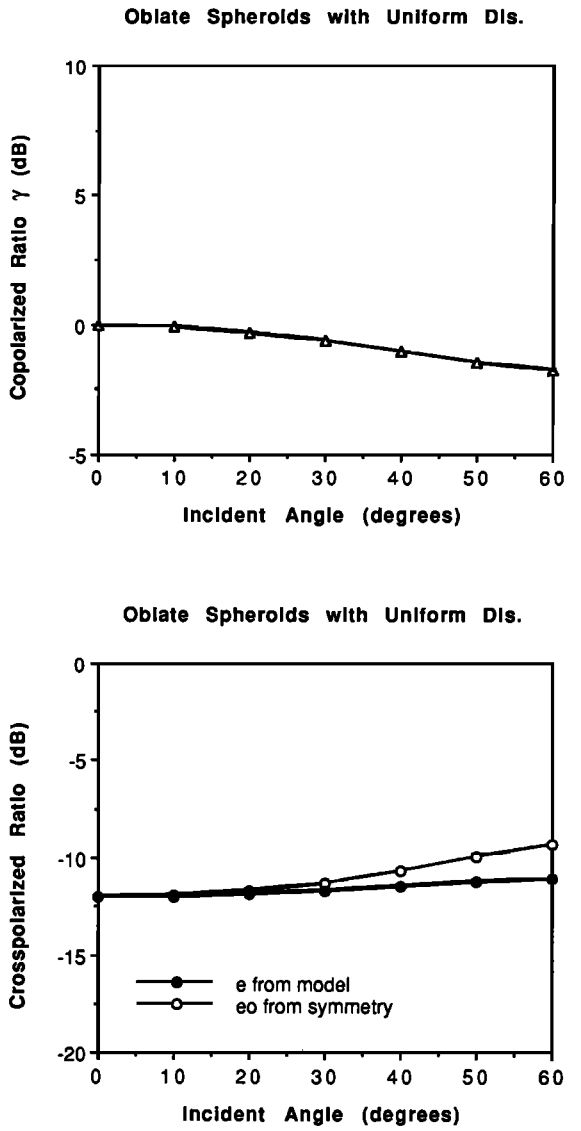

Fig. 5. Polarimetric response of oblate spheroids with uniform distribution of orientation.

and e smaller than e_0 except at normal incidence where $e = e_0$. This is because both needles and disks are more horizontally oriented according to planophile distribution.

3.4. *Plagiothile Distribution*

Plagiothile distribution of orientation depicts oblique scatterers as most frequent. As functions of inclination angle, the plagiothile probability density and distribution can be written as

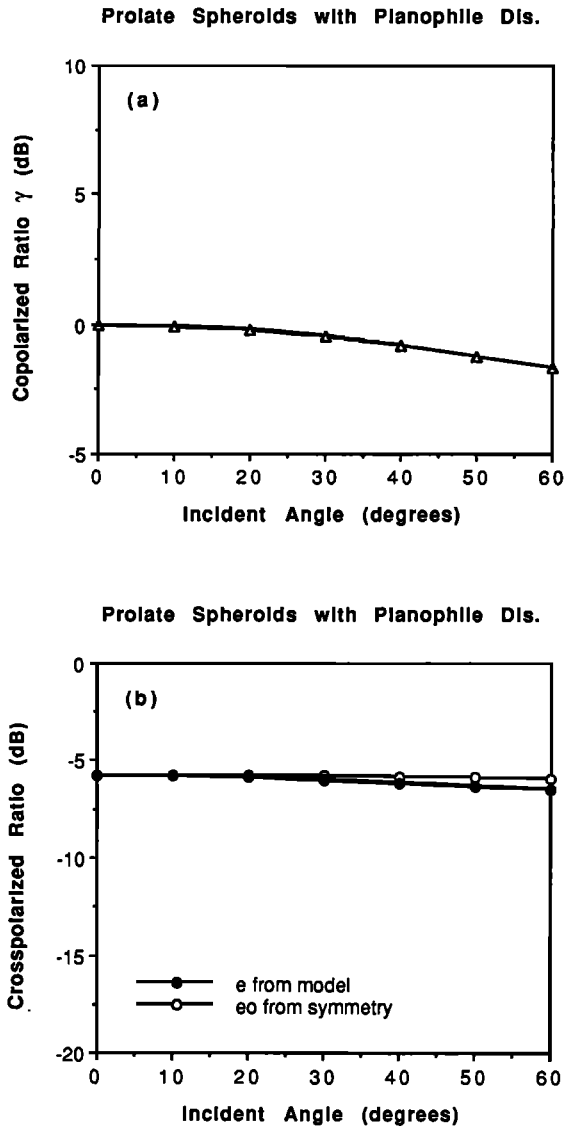

Fig. 6. Polarimetric response of prolate spheroids with planophile distribution of orientation.

Density

$$p(\theta) = 2(1 - \cos 4\theta)/\pi \tag{7a}$$

Distribution

$$P(\theta) = (4\theta - \sin 4\theta)/(2\pi) \tag{7b}$$

The density function (7*a*) is used to graph the plagiothile probability density in the polar coordinates for variable inclination angle in Figure 1*d*, where the solid dots indicate values of the density for inclination angles from 0 to $\pi/2$ (0°, 90°).

Permittivity $\varepsilon = (30 + i10)\varepsilon_0$ at 5.3 GHz is also assumed for the scatterers as in the previous cases to calculate the scattering coefficients from the model. On the basis of calculated coefficients, e_0 is then obtained from (3). Figure 8 presents the results for needlelike scatterers and in Figure 9 for disklike scatterers. As the incident angle increases, copolarized ratio γ increases for needles and decreases for disks. The behaviors in e and e_0 are also different

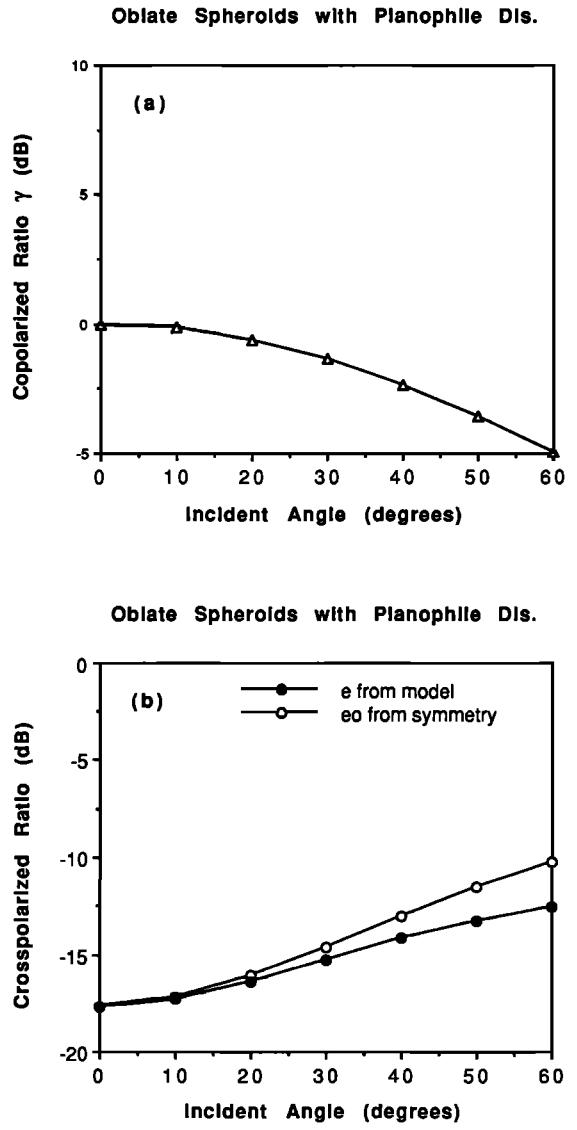

Fig. 7. Polarimetric response of oblate spheroids with planophile distribution of orientation.

for the two types of scatterers. In the case of needles, e is larger and e_0 is smaller as incident angle increases. For disks, $e \geq e_0$, and both have an increasing trend. However, the values of e and e_0 are close. Thus for oblique orientations most frequent, needlelike scatterers behave more differently from the randomly oriented scatterers compared to disklike scatterers.

3.5. *Erectophile Distribution*

Erectophile distribution of orientation is used for scatterers with dominantly vertical orientations.

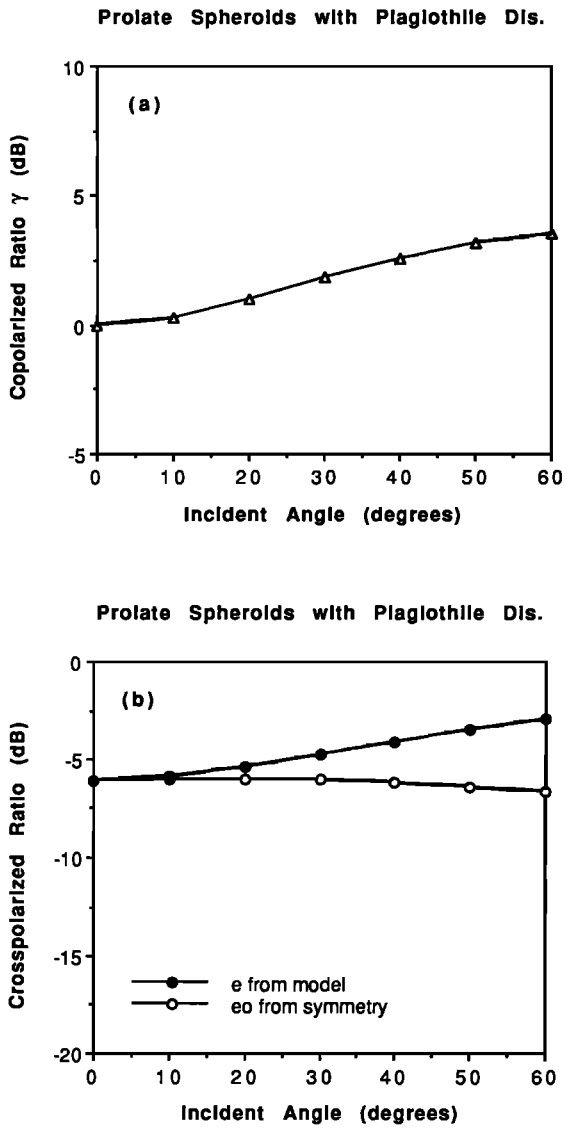

Fig. 8. Polarimetric response of prolate spheroids with plagiothile distribution of orientation.

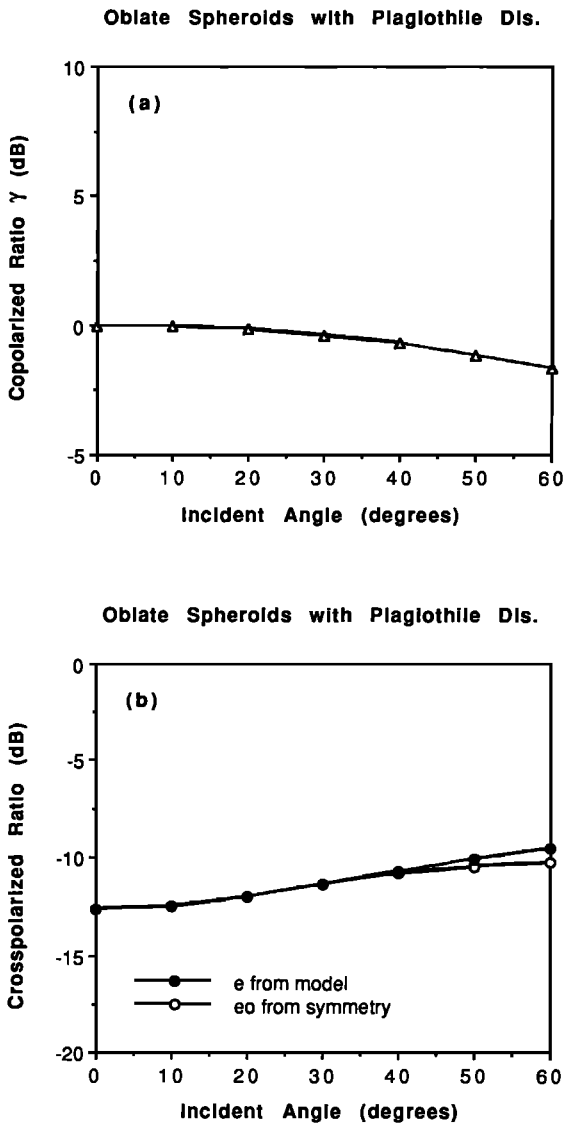

Fig. 9. Polarimetric response of oblate spheroids with plagiothile distribution of orientation.

The probability density and distribution for erectophile orientation are related to the inclination angle in the following manners:

Density

$$p(\theta) = 2(1 - \cos 2\theta)/\pi \tag{8a}$$

Distribution

$$P(\theta) = (2\theta - \sin 2\theta)/\pi \tag{8b}$$

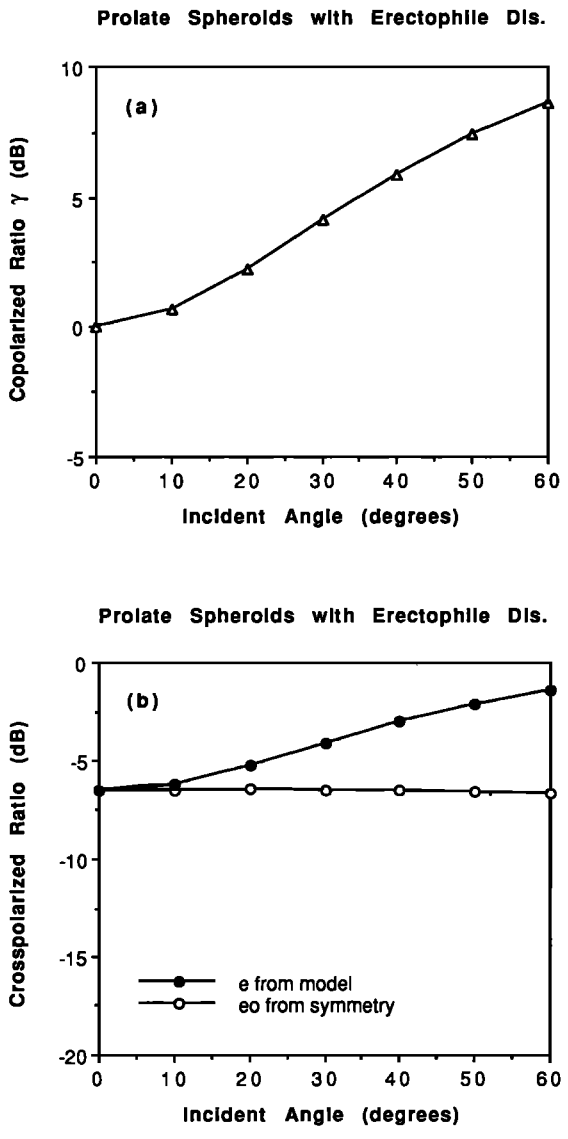

Fig. 10. Polarimetric response of prolate spheroids with erectophile distribution of orientation.

The density function (8*a*) is illustrated with the plot in Figure 1*e* in polar coordinates for inclination angles in the range from 0 to $\pi/2$ (0°, 90°) denoted by the solid dots.

Polarimetric scattering coefficients are calculated with the model for scatterers with the same permittivity $\varepsilon = (30 + i10)\varepsilon_0$ at 5.3 GHz. The relevant parameters are then substituted in (3) to find the corresponding value for e_0. Results for needlelike scatterers and disklike scatters are shown in Figures 10 and 11, respectively. When incident angle becomes larger, γ increases faster for needles compared to the case for discs. While e_0 decreases at larger incident angles, e quickly increases for needles and slowly decreases for disks. Similarly to the plagiothile distribution, the needlelike scatterers, as compared to disklike scatterers, with erectophile distribution have characteristics that further depart from the random orientation behavior.

3.6. *Extremophile Distribution*

Extremophile distribution of orientation is prescribed for scatterers with oblique orientations least

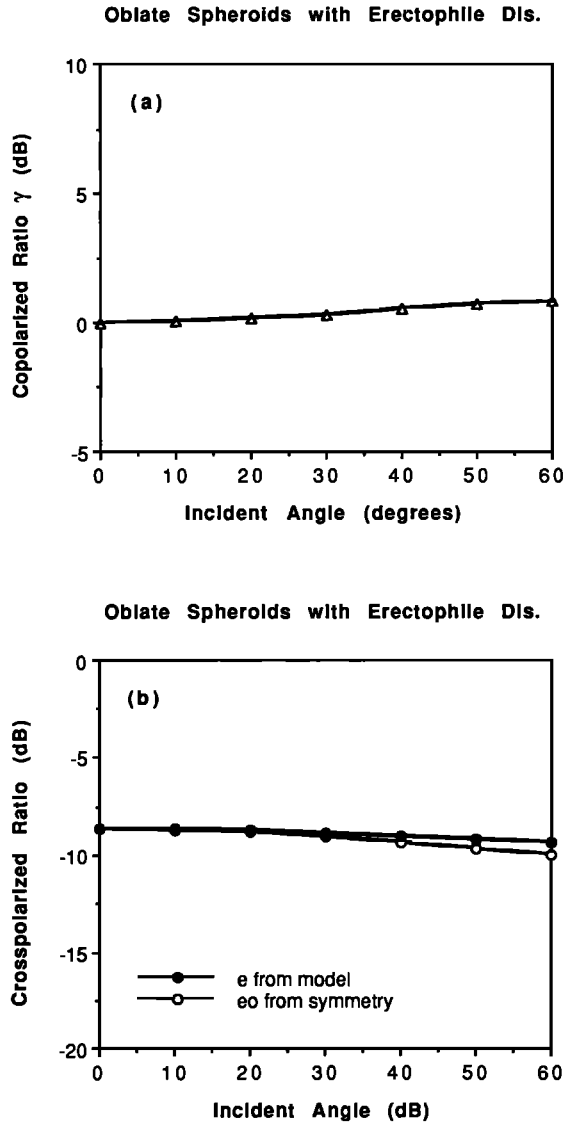

Fig. 11. Polarimetric response of oblate spheroids with erectophile distribution of orientation.

frequent. In this case the probability density and distribution are dependent on the inclination angle as follows:

Density

$$p(\theta) = 2(1 + \cos 4\theta)/\pi \tag{9a}$$

Distribution

$$P(\theta) = (4\theta + \sin 4\theta)/(2\pi) \tag{9b}$$

Function (9*a*) is used to plot the extremophile probability density in the polar coordinates for variable inclination angle in Figure 1*f* where the solid dots represent values of the density for inclination angles from 0 to $\pi/2$ (0°, 90°).

Permittivity $\varepsilon = (30 + i10)\varepsilon_0$ for the scatterers is taken at 5.3 GHz as in the other cases to calculate the scattering coefficients. From the calculated coefficients, e_0 is then obtained by using (3). Figures 12 and 13 show the results for needlelike scatterers, and for disklike scatterers, respectively. When incident angle increases, copolarized ratio γ increases for needles and decreases for disks. For both types of scatterers, e decreases and e_0 increases as a function of incident angle.

3.7. *Identification of Scatterer Orientations*

Identification of scatterer orientations will help classify medium types, study environmental effects on the media, and recognize variations in physiologic states. For needlelike scatterers, the orientation distributions are arranged from more horizontal to more vertical orientation as extremophile, planophile, spherical, uniform, plagiothile, and erectophile, respectively. The arrangement for the orientation of disklike scatterers from horizontal to vertical is extremophile, planophile, uniform, spherical, plagiothile, and erectophile. In general, the horizontal-to-vertical ordering of the distributions under consideration are the same for both scatterer types except the uniform distribution. This distribution, as defined by (5), is preferentially vertical for needles and horizontal for disks. To identify the scatterer orientations, the information conveyed in the polarimetric scattering coefficients need to be extracted by using a certain parameter which behaves consistently with the horizontal-to-vertical ordering of the distributions.

Behaviors of polarimetric scattering coefficients

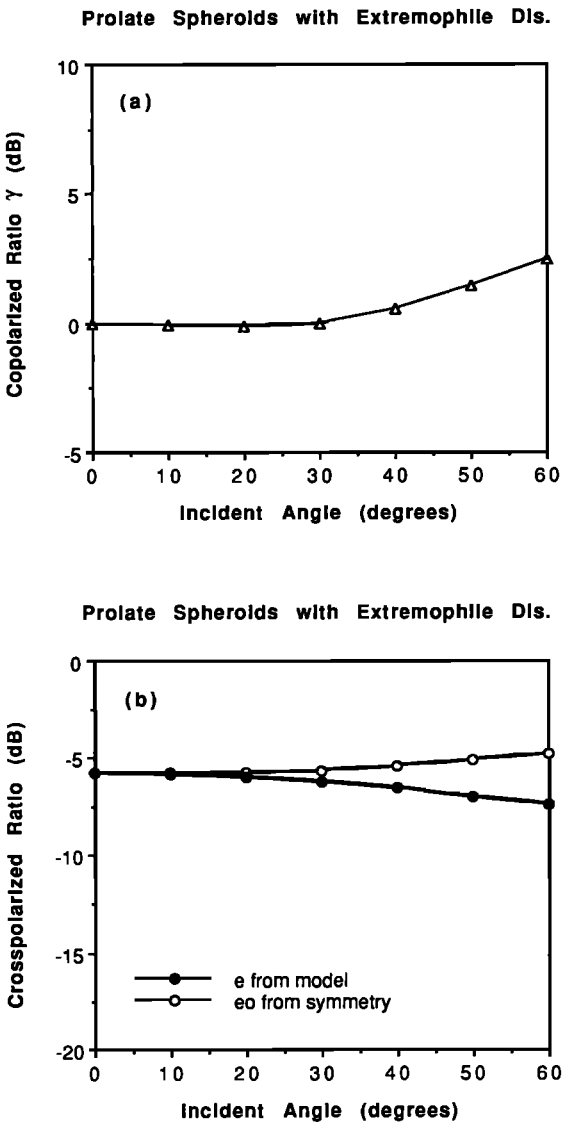

Fig. 12. Polarimetric response of prolate spheroids with extremophile distribution of orientation.

have been investigated in the above subsections for various types of scatterer orientation distributions. It is observed from the plots in this section that e appears to have smaller values for more horizontal needles at large incident angles. The behavior of e for disk, however, does not seem to have the same trend. Furthermore, γ and $|\rho|$ do not directly reveal the orientation structure since their values do not show a trend corresponding to the horizontal-to-vertical classification of the distribution. In all cases the phase of ρ is small and may not be useful for

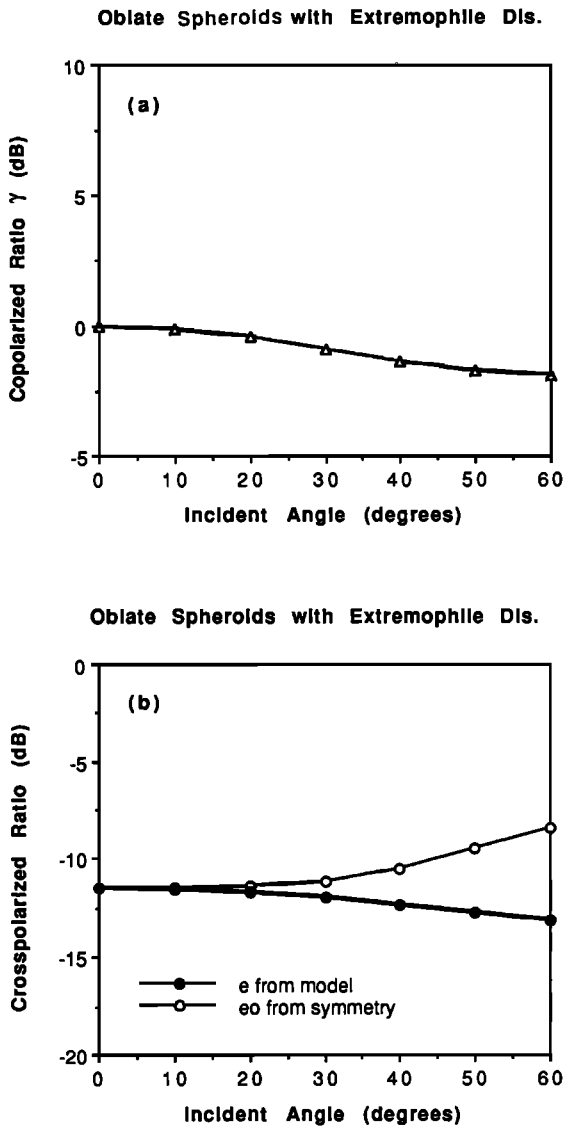

Fig. 13. Polarimetric response of oblate spheroids with extremophile distribution of orientation.

identification of the inclination orientation. A new parameter is therefore necessary to be obtained such that its trend discriminates the orientation in a consistent manner regardless of the scatterer shapes. For this purpose, the quantity δ_e is defined as follows:

$$\delta_e = \frac{e}{e_0} = \frac{2e}{1-|\rho|} = \frac{2\sigma_{hvhv}\sqrt{\sigma_{vvvv}}}{\sigma_{hhhh}\sqrt{\sigma_{vvvv}} - |\sigma_{hhvv}|\sqrt{\sigma_{hhhh}}} \tag{10}$$

In Figure 14, δ_e ratios are plotted as functions of incident angles for both needles and disks with all of the orientation distributions under consideration. It is seen from Figure 14*a* that δ_e for the needlelike scatterer becomes larger when the distributions change in the order of extremophile, planophile, spherical, uniform, plagiothile, and erectophile, which is exactly the horizontal-to-vertical ordering discussed in the last paragraph. From Figure 14*b* for disks, δ_e has the same trend except that the pla-

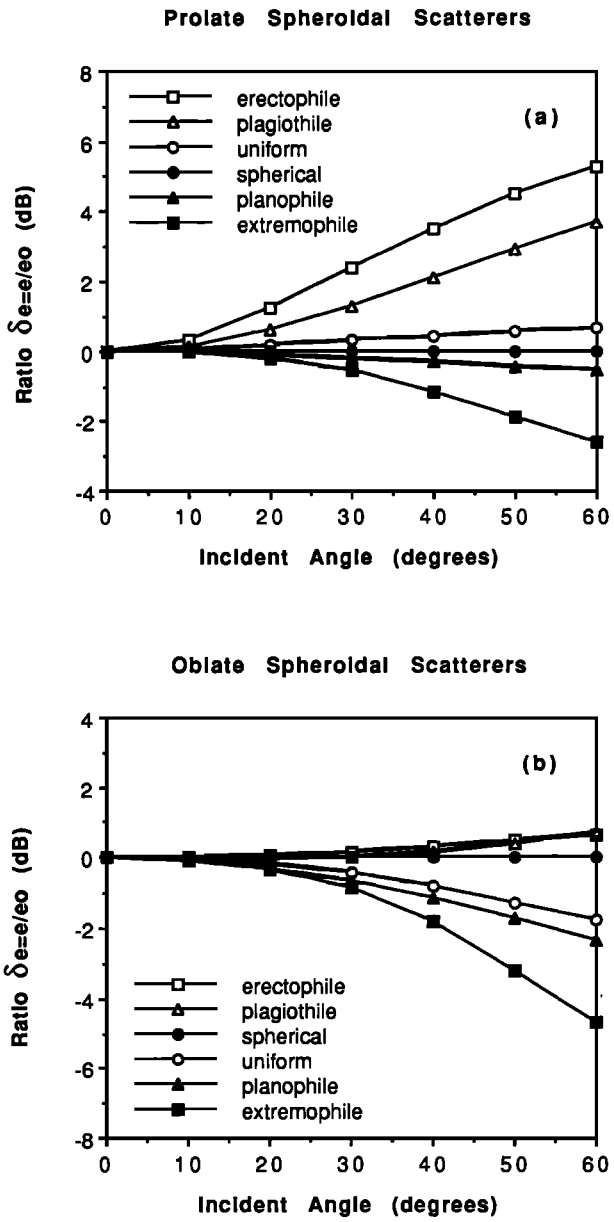

Fig. 14. The quantity δ_e as a function incident angle for prolate (a) and oblate (*b*) spheroids.

Plate 1. SAR image of scene 1197 acquired over a coniferous forest in Mount Shasta.

giothile and erectophile cases are very close. The simulation is also carried out for long dielectric cylinders of 15.0 cm in length and 1.5 mm in diameter; the same conclusion for δ_e is reached. For larger disks of 5.0 cm in diameter and 0.2 mm in thickness, the simulation indicates that $\delta_e < 1$ for the horizontal disks and $\delta_e > 1$ for the vertical. The quantity δ_e can thus be used to identify the scatterer orientation regardless of the needlelike or disklike shape. Furthermore, the identification can be more definitive at larger incident angles since the curves for δ_e become further diverse. This phenomenon is due to the departure from the azimuthal symmetry of the scattering medium when the incident angle increases.

4. EXPERIMENTAL OBSERVATIONS

Polarimetric data at microwave frequencies acquired with the Jet Propulsion Laboratory (JPL) airborne synthetic aperture radar (SAR) over forests, sea ice, and sea surface are used to illustrate the application of symmetry properties to obtain structural information of the scattering media. In this section, coniferous forest in the Mount Shasta area, mixed forest near Presque Isle, sea ice in the Beaufort Sea, and sea surface in the Bering Sea are investigated. Comparisons between e and e_0, or equivalently the value of δ_e, at P, L, and C band frequencies are made to infer the structures of the media. A selection of distributed targets can be made for applications to calibrations of polarimetric radars. All images under consideration here are calibrated from high-resolution data in the scattering matrix format.

4.1. *Forests*

SAR images have been acquired for various forest types. In this section, polarimetric data for a coniferous forest and a mixed forest are studied. In June 1989, SAR images were obtained over Mount Shasta in northern California. Mount Shasta scene 1197 (JPL catalog number) is shown in Plate 1 where a section of Mount Shasta is seen in the

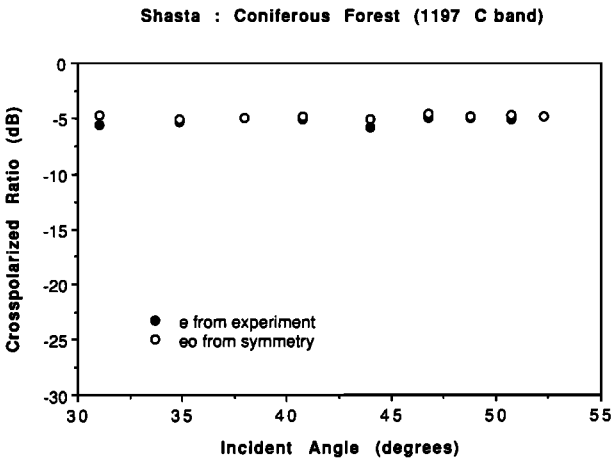

Fig. 15. Cross-polarized ratio e and e_0 versus incident angles at C band for coniferous forest in Shasta scene 1197.

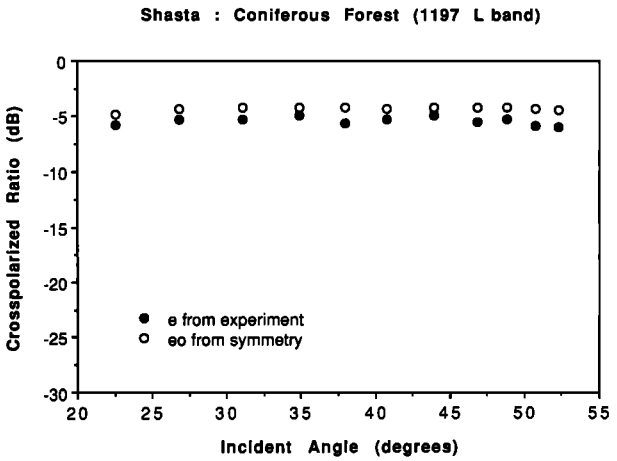

Fig. 16. Cross-polarized ratio e and e_0 versus incident angles at L band for coniferous forest in Shasta scene 1197.

upper right part of the image. This site is mostly covered by forest, and small dark areas are clear cuts where some corner reflectors are located. Forested areas in Mount Shasta are dominated by ponderosa pine and white fir species [*Zebker et al.*, 1991]. The scattering matrix data are first symmetrized with a new algorithm based on the principle of reciprocity [*Yueh et al.*, 1993]. Since the forest does not have azimuthal preference or alignment, the reflection symmetry is used to remove the channel cross talk (S. H. Yueh, et al., External calibration of polarimetric radars using distributed targets, submitted to *IEEE Transactions on Geoscience and Remote Sensing*, 1992). The corner reflectors are then used to check the channel imbalance for both magnitude and phase. Eleven areas, each containing about 1000 pixels, in the Shasta forest are selected to extract the covariance matrices for incident angles spanning from 22.5° to 52.3°. In Figure 15, e and e_0 at C band are compared. It is observed that $e \approx e_0$ from the plot. The data also show that $\gamma \approx 0$ dB and Im $\rho \approx 0$. When the equalities are exact, these relations are the direct consequence of the centrical symmetry due to the random orientation of the vegetation elements described by spherical distribution as discussed in the last section. Thus as seen by the C band polarimetric SAR, the forest canopies contain scatterers whose orientation is random. Figure 16 presents the results for e and e_0 at L band where e is about 1 dB lower than e_0 at most incidence angles and 2 dB lower at incident angles around 50°. This is because L band waves can penetrate the forest foliage, and the departure from centrical symmetry of the scattering configuration is due to the horizontal orientation of the branches or other vegetation elements with a preferential orientation.

In July 1990, the Forest Penetration (FOPEN) Experiment campaign was carried out, and polarimetric backscattering data were collected over a forested area near Presque Isle, Maine. Presque Isle Scene 1406 is shown in Plate 2 where the forest has bright returns, the elongated dark area on top of the image is the Little Machias Lake, and the dark area near the road in the middle left part contains corner reflectors and other calibration targets. The forest is a mix of coniferous trees such as spruce, balsam fir, and cedar; and deciduous trees such as birch, maple, and aspen. The calibration procedures are done in the similar manner as for scene 1197. Covariance matrices are then extracted for forest from 34.4° to 55.4° incidence. At C band, e is close to e_0 and becomes smaller than e_0 when the frequency decreases to L band and then to P band as seen in Figures 17, 18, and 19, respectively. Thus forests behave especially at C band well in accordance with the characteristics of the centrical symmetry which can be used to calibrate channel imbalance for spaceborne sensors such as SIR-C and EOS after the cross talk is removed with reflection symmetry without the deployment of man-made calibration targets.

4.2. *Sea Ice*

Polarimetric SAR scenes of sea ice in the Beaufort Sea were acquired during March 1988 in a

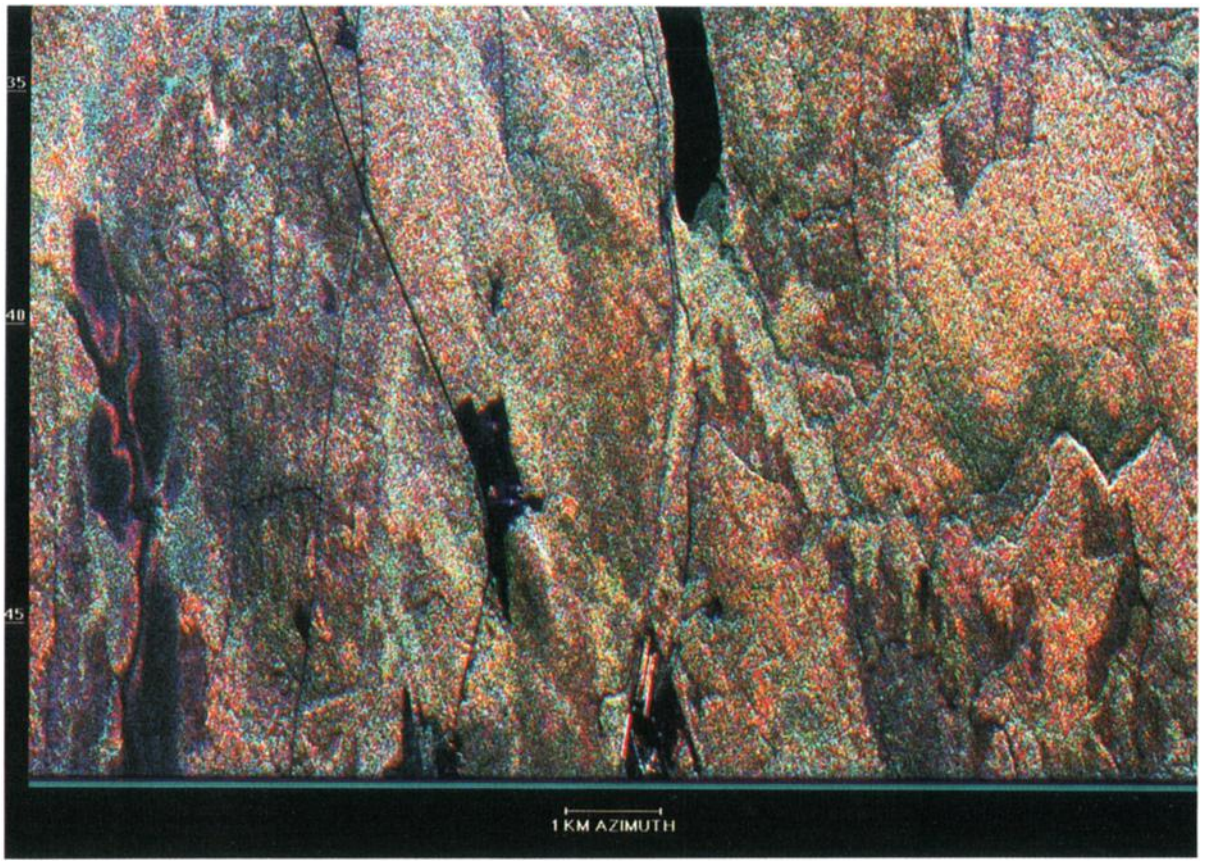

Plate 2. SAR image of scene 1406 acquired over a mixed forest near Presque Isle, Maine.

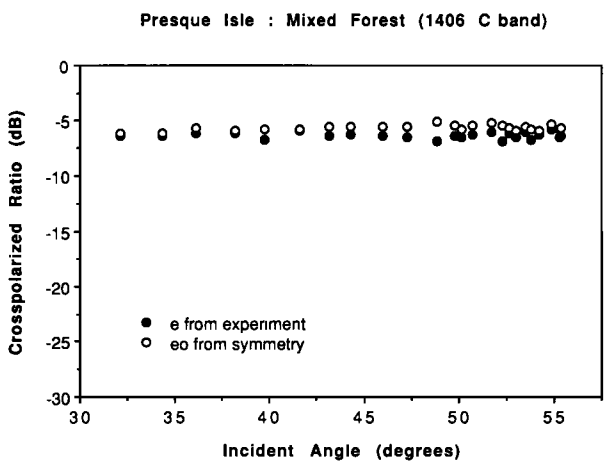

Fig. 17. Cross-polarized ratio e and e_0 versus incident angles at C band for mixed forest in Presque Isle scene 1406.

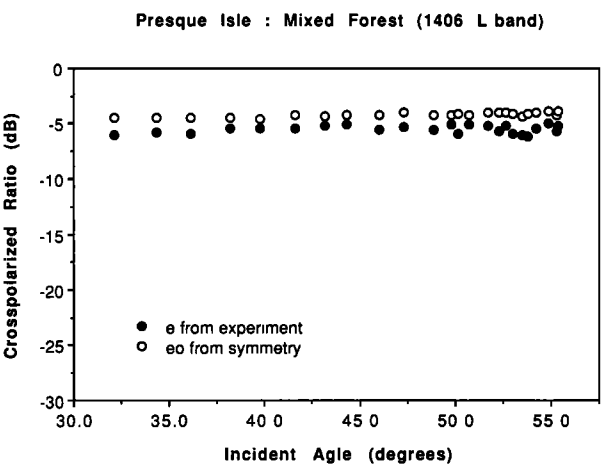

Fig. 18. Cross-polarized ratio e and e_0 versus incident angles at L band for mixed forest in Presque Isle scene 1406.

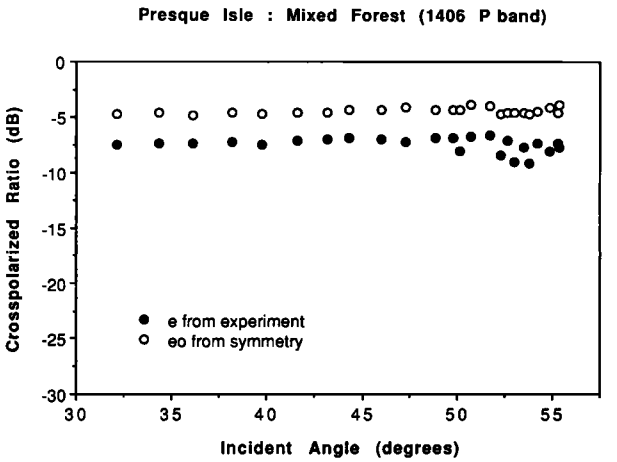

Fig. 19. Cross-polarized ratio e and e_0 versus incident angles at P band for mixed forest in Presque Isle scene 1406.

series of NASA DC-8 airborne flights [*Cavalieri*, 1988]. Weather and sea ice characteristic data were recorded at the Applied Physics Laboratory's drifting ice station northeast of Prudhoe Bay, Alaska. Meteorological and ice measurements were reported [*Wen et al.*, 1989]. The sea ice scenes consisted of a transition from the extensive coastal first-year ice region to multiyear ice pack to the north. First-year ice near the ice station was 1.5 m to 2.4 m thick and was covered by a snow layer of 15.0-cm average depth. Multiyear ice was also covered by snow and hummocked up to 6.0 m height.

Beaufort scene 0183 in Plate 3 contains floes of multiyear ice with bright backscatters. The dark part on the left of the image is first-year sea ice. The

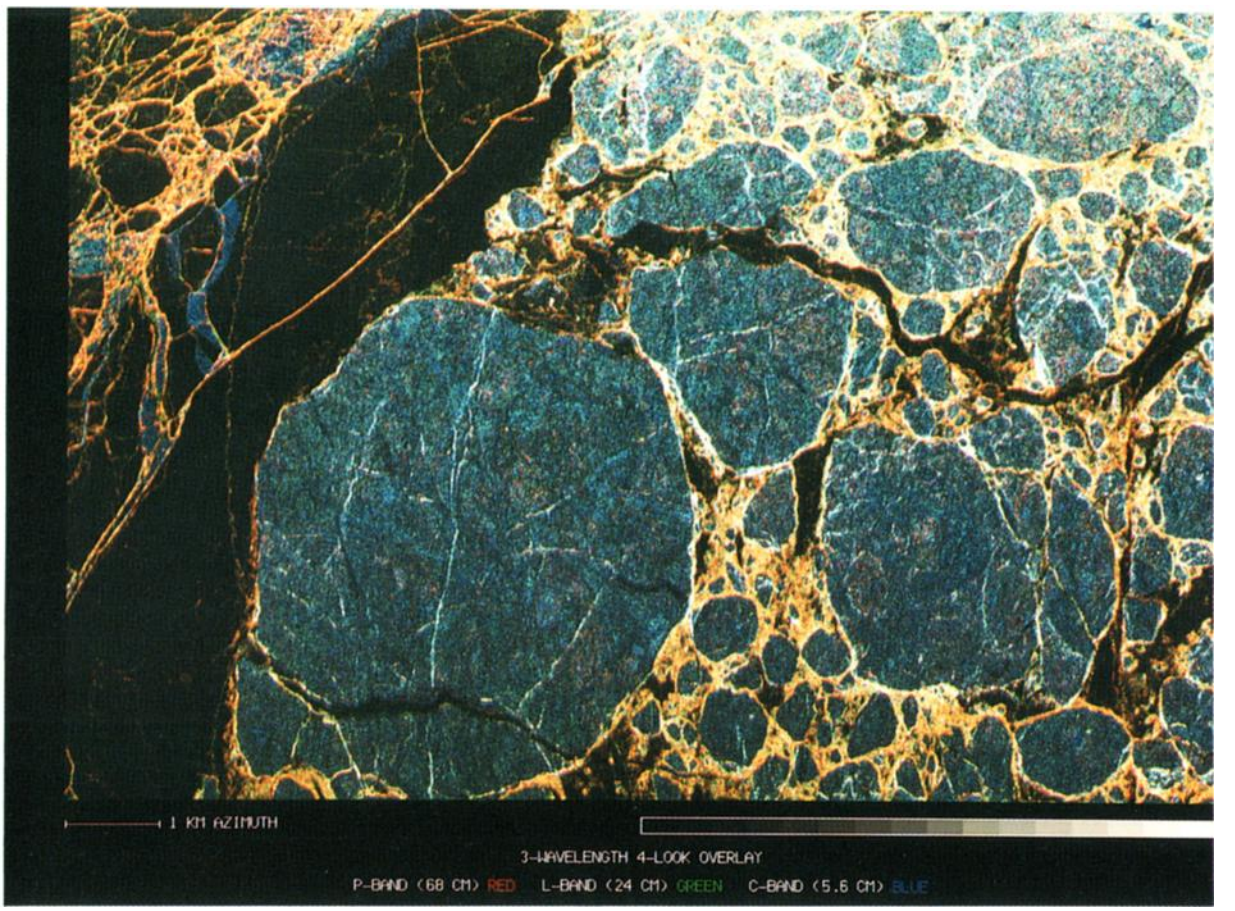

Plate 3. SAR image of scene 0183 acquired over sea ice in Beaufort Sea.

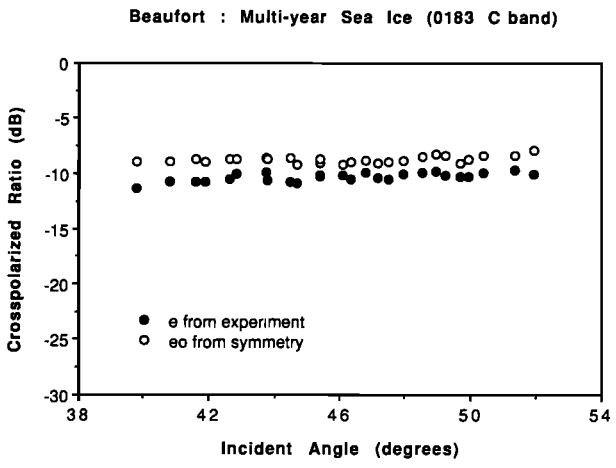

Fig. 20. Cross-polarized ratio e and e_0 versus incident angles at C band for multiyear sea ice in Beaufort scene 0183.

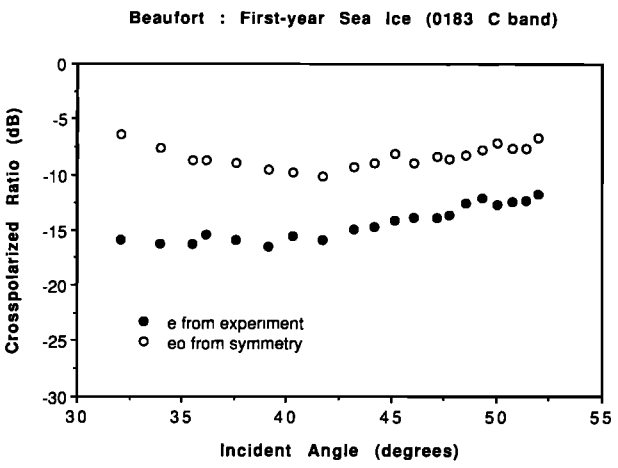

Fig. 21. Cross-polarized ratio e and e_0 versus incident angles at C band for first-year sea ice in Beaufort scene 0183.

scattering matrix data are symmetrized based on reciprocity, and the cross talk are removed with the reflection symmetry. The channel imbalance is checked by comparing the signatures of multiyear sea ice nearer to normal incidence with the imbalance obtained from other scene with the relative uncertainty less than 1 dB. The cross-polarized ratio e and e_0 at C band are plotted versus incident angles in Figure 20 for multiyear ice. It is observed that multiyear ice has e about a couple of decibels lower than e_0. Scattering from multiyear sea ice is caused by the hummocky topography and the randomly oriented air inclusions. In this case, both surface and volume scattering mechanisms give rise to signatures with properties approaching the characteristics of the centrical symmetry [*Nghiem et al.*, 1992]. This explains the proximity between e and e_0 of multiyear sea ice. Figure 21 shows that e is 5 to 10 dB lower than e_0 for first-year ice at C band. Structurally, first-year ice has a preferential vertical orientation of brine inclusions [*Weeks and Ackley*, 1982] due to the columnar growth of the ice resulting in the vertical anisotropy. The anisotropy and the boundary effect, which destroy the centrical symmetry, can cause the large difference between e and e_0 [*Nghiem et al.*, 1992]. L band results for the cross-polarized ratio e and e_0 for multiyear and first-year sea ice are shown in Figures 22 and 23, respectively. The observed trends of e and e_0 are similar to the corresponding C band cases, except that the relative differences between e and e_0 are larger. These observations are also confirmed by the polarimetric data at both L and C band frequencies from Beaufort scene 1372, which was also acquired on the same date at a different location. From this analysis, the results indicate that first-year ice signatures depart significantly from centrical symmetry behavior as compared to multiyear ice as evident in the behavior of e and e_0 due to the difference in the structures of the ice types.

4.3. *Sea Surface*

During a flight over the Bering Sea also in March 1988, SAR scenes were collected over sea ice and sea surface. Bering scene 0259 is chosen for the investigation of polarimetric scattering from sea surface. This scene is selected for the unique op-

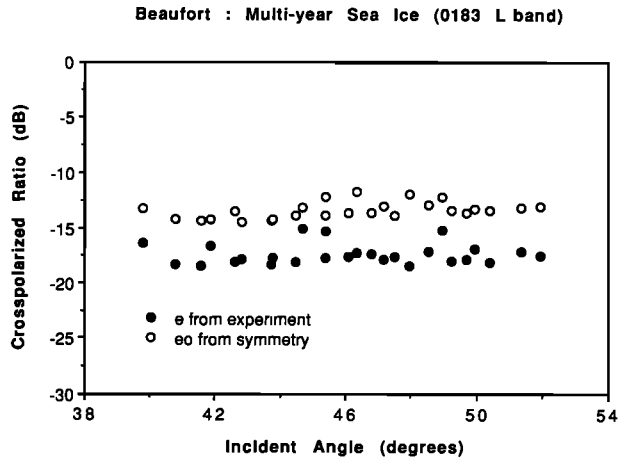

Fig. 22. Cross-polarized ratio e and e_0 versus incident angles at L band for multiyear sea ice in Beaufort scene 0183.

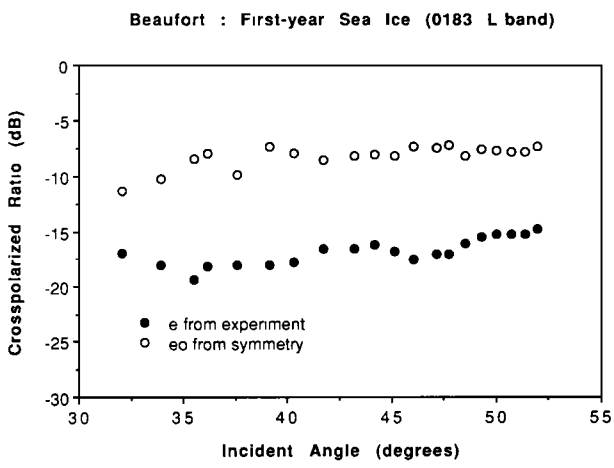

Fig. 23. Cross-polarized ratio e and e_0 versus incident angles at L band for first-year sea ice in Beaufort scene 0183.

portunity provided by the medium types included in the image allowing the cross talk removal. As shown in Plate 4, Bering scene 0259 shows mostly sea surface; however, a significant portion of sea ice is seen on the left of the image. Sea surface may not have the reflection symmetry, needed to remove the cross talk, when the radar-looking direction does not coincide with the wave or wind direction. Therefore the sea ice portion in the image is particularly useful for the cross talk removal. After the calibration procedures are carried out for the high-resolution data, 18 areas on the sea surface are used to extract the covariance matrices with incident angles from 35.4° to 51.7°. The results of e and e_0 at L band are shown in Figure 24. Both e and e_0 increase as incident angles increase and e becomes larger than e_0 at large incident angles. Interestingly, in this case, e is higher than e_0 at all incident angles, and the difference becomes larger as incident angle increases. This phenomenon is due to the preferential alignment of the surface scatterers in the wave or wind direction and can be explained by using a two-scale rough surface model with two-dimensional perturbations on quasi-periodic wave surface [*Yueh et al.*, 1989]. This observation suggests a

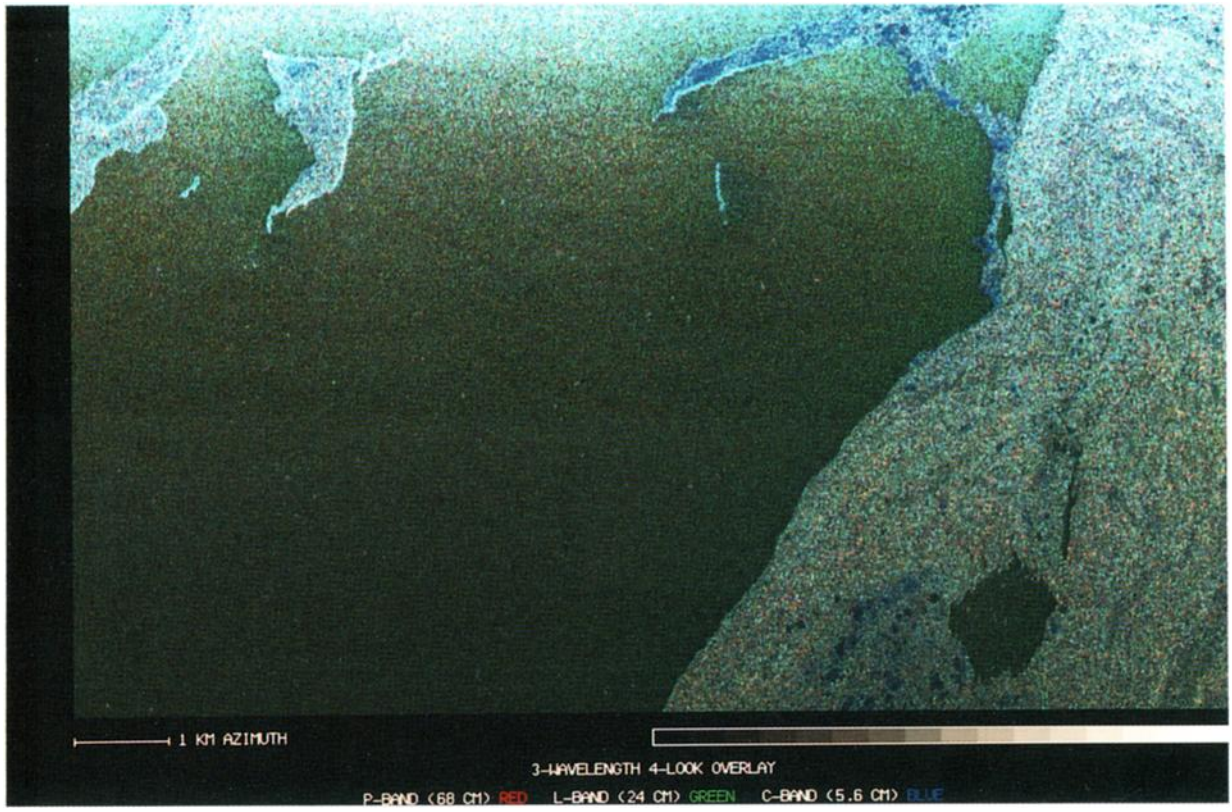

Plate 4. SAR image of scene 0259 acquired over sea surface in the Bering Sea.

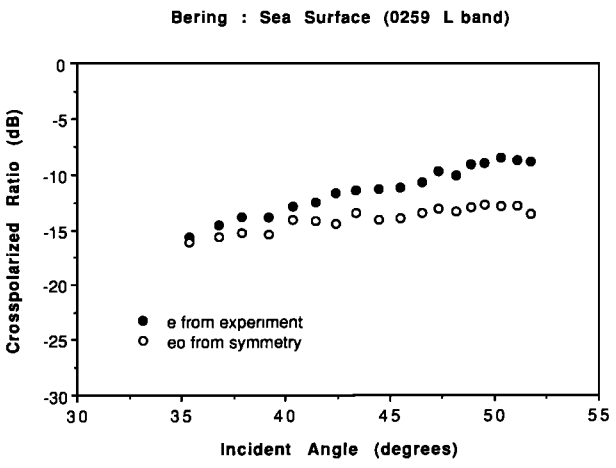

Fig. 24. Cross-polarized ratio e and e_0 versus incident angles at L band for sea surface in Bering scene 0259.

direction for further investigation with rough surface models.

5. SUMMARY AND DISCUSSIONS

In this paper, geophysical medium structures are investigated with polarimetric backscatters based on symmetry properties. First, the polarimetric characteristics of symmetrical configurations are reviewed. Various orientation distributions of nonspherical scatterers are then examined to study their effects on polarimetric backscattering coefficients. A new parameter δ_e is defined to study scattering structures in geophysical media. The volume-scattering model indicates that $\delta_e = 1$ for randomly oriented scatterers, $\delta_e < 1$ for preferentially horizontal scatterers, and $\delta_e > 1$ for preferentially vertical scatterers.

Experimental observations are then presented for results from polarimetric data sets at P, L, and C band frequencies acquired with the Jet Propulsion Laboratory (JPL) airborne synthetic aperture radar (SAR). The SAR images include forests, sea ice, and sea surface. For forests, coniferous forest in Mount Shasta, and mixed forests near Presque Isle are considered. The results show evidence of the centrical symmetry in forest canopies at C band frequency. At L band and P band, the departure from the centrical characteristics is due to preferential orientation of vegetation elements in the forests. For sea ice the scenes are in the Beaufort Sea containing various ice types. Multiyear sea ice has the cross-polarized ratio e close to e_0, while the difference between the two parameters is large for first-year sea ice. This is due to the randomness in the scattering structure of multiyear sea ice, while first-year sea ice has a preferential alignment in the vertical columnar structure of the ice. For a sea surface in the Bering Sea it is observed e and e_0 at L band increase with increasing incidence and $e > e_0$ caused by directional sea surface waves. From this study it is shown that information regarding the structures of the media can be inferred from δ_e or e compared with e_0.

For polarimetric calibration, symmetry properties of geophysical media are useful. A new method for calibrating polarimetric radar images using only the responses from natural distributed targets has been developed (S. H. Yueh, et al., External calibration of polarimetric radars using distributed targets, submitted to *IEEE Transactions on Geoscience and Remote Sensing*, 1992). After the reciprocity is applied to symmetrize the polarimetric data, cross talk parameters are estimated based on the responses from distributed targets with reflection symmetry. This cross talk removal can be carried out for virtually all images since many geophysical media exhibit the reflection symmetry. The phase and amplitude of the channel imbalance are then determined by distributed targets with rotation symmetry. The analyses on the polarimetric SAR data presented in this paper can provide directions in the selection of distributed targets for polarimetric calibration. For cross talk removal, a distributed target with reflection symmetry is necessary, but any accompanying rotation symmetry can inflict uncertainty on the derived cross talk parameters; this means sea ice with e more different than e_0 is a better candidate for the cross talk estimation. For the relative phase and amplitude calibration, the data at C band show that forests still well possess centrical symmetry behavior at rather large incident angles; this indicates the calibration can be done at oblique incidence. The new calibration technique has been applied to polarimetric data collected by JPL SAR and will be useful for calibration of spaceborne polarimetric sensors.

Acknowledgments. The research described in this paper was carried out at the Jet Propulsion Laboratory, California Institute of Technology, under a contract with the National Aeronautics and Space Administration. The authors thank Y. L. Lou, S. L.

Durden, E. J. Rignot, and J. P. Crawford of JPL for their help in acquiring the data used in this paper.

REFERENCES

Cavalieri, D. J., NASA sea ice and snow validation program for the DMSP SSM/I: NASA DC-8 flight report, *NASA Tech. Memo. 100706*, 1988.

Goel, N. S., and D. E. Strebel, Simple beta distribution representation of leaf orientation in vegetation canopy, *Agron. J.*, *76*, 800–802, 1984.

Hamermesh, M., *Group Theory and Its Application to Physical Problems*, Addison-Wesley, Reading, Mass., 1972.

Kimes, D. S., J. A. Smith, and J. K. Berry, Extension of the optical analysis technique for estimating forest canopy geometry, *Aust. J. Bot.*, 27, 575–588, 1979.

Le Toan, T., A. Beaudoin, D. L. S. Chong, J. A. Kong, S. V. Nghiem, and H. C. Han, Active microwave remote sensing of vegetation, *Eur. Space Agency Rep. 8447/89/NL/PB(SC)*, 1990.

Nghiem, S. V., S. H. Yueh, R. Kwok, and F. K. Li, Symmetry properties in polarimetric remote sensing, *Radio Sci.*, *27*(5), 693–711, 1992.

Stewart, R. H., *Methods of Satellite Oceanography*, University of California Press, Berkeley, 1985.

Tsang, L., J. A. Kong, and R. T. Shin, *Theory of Microwave Remote Sensing*, chap. 3, 119–217, John Wiley, New York, 1985.

Weeks, W. F., and S. F. Ackley, *The Growth, Structure, and Properties of Sea Ice, Monogr. Ser.*, vol. 82-1, U.S. Army Corps of Engineers, Cold Regions Res. and Eng. Lab., 1982.

Wen, T., W. J. Felton, J. C. Luby, W. L. J. Fox, and K. L. Kientz, Environmental measurements in the Beaufort Sea, spring 1988, *Tech. Rep., APL-UW TR 8822*, Applied Phys. Lab., Univ. of Wash., Seattle, 1989.

Yueh, H. A., R. T. Shin, and J. A. Kong, Scattering from randomly perturbed periodic and quasiperiodic surfaces, *Progress in Electromagnetics Research*, edited by J. A. Kong, vol. 1, chap. 4, pp. 297–358, Elsevier, New York, 1989.

Yueh, S. H., S. V. Nghiem, and R. Kwok, Symmetrization of cross-polarized responses in polarimetric radar images using reciprocity, *IEEE Trans. Geosci. Remote Sens.*, in press, 1993.

Zebker, H. A., J. J. van Zyl, S. L. Durden, and L. Norikane, Calibrated imaging radar polarimetry: Technique, examples, and applications, *IEEE Trans. Geosci. Remote Sens.*, *29*(6), 942–961, 1991.

R. Kwok, S. V. Nghiem, D. T. Nguyen, and S. H. Yueh, Jet Propulsion Laboratory, Mail Stop 300-235, 4800 Oak Grove Drive, Pasadena, CA 91109.